CDK5/p35-dependent microtubule reorganization contributes to homeostatic shortening of the axon initial segment

[$]Israt Jahan, [$]Ryota Adachi, Ryo Egawa, Haruka Nomura, Hiroshi Kuba*

Department of Cell Physiology, Graduate School of Medicine, Nagoya University, Nagoya 466-8550, Japan

Abbreviated title (44 / 50 characters)

CDK5/p35 mediates homeostatic AIS plasticity

[$]These authors contributed equally to this work.

*Correspondence: kuba@med.nagoya-u.ac.jp

Number of pages: 36

Number of Figures: 7, Table: 1

Number of words in Abstract: 220, Introduction: 640, Discussion: 1383

Conflicts of Interest:

The authors declare no competing financial interests.

Acknowledgements:

This work was supported by Grants-in-aid from MEXT (19H04747, 21H02577 to H.K.); the Takeda Science Foundation to H.K. We thank the Division for Medical Research Engineering, Nagoya University Graduate School of Medicine, for usage of NanoDrop 2000, Agilent 2100 Bioanalyzer, and Mx3005P QPCR system.

Abstract

The structural plasticity of the axon initial segment (AIS) contributes to the homeostatic control of activity and optimizes the function of neural circuits; however, the underlying mechanisms are not fully understood. In this study, we prepared a slice culture containing nucleus magnocellularis from chickens of both sexes that reproduces most features of AIS plasticity *in vivo*, regarding its effects on characteristics of AIS and cell-type specificity, and revealed that microtubule reorganization via activation of CDK5 underlies plasticity. Treating the culture with a high-K^+ medium shortened the AIS and reduced sodium current and membrane excitability, specifically in neurons tuned to high-frequency sound, creating a tonotopic difference in AIS length in the nucleus. Pharmacological analyses revealed that this AIS shortening was driven by multiple Ca^{2+} pathways and subsequent signaling molecules that converge on CDK5 via the activation of ERK1/2. AIS shortening was suppressed by overexpression of dominant-negative CDK5, whereas it was facilitated by the overexpression of p35, an activator of CDK5. Notably, p35(T138A), a phosphorylation-inactive mutant of p35, did not shorten the AIS. Moreover, microtubule stabilizers occluded AIS shortening during the p35 overexpression, indicating that CDK5/p35 mediated AIS shortening by promoting disassembly of microtubules at distal AIS. This study highlights the importance of microtubule reorganization and regulation of CDK5 activity in structural AIS plasticity and the tuning of AIS characteristics in neurons.

Key words

Axon initial segment, plasticity, microtubules, CDK5, p35, Ca^{2+}

Significant Statement

The structural plasticity of AIS strongly impacts the output of neurons and plays a fundamental role in the physiology and pathology of the brain. However, the mechanisms linking neuronal activity to structural changes in AIS are not well understood. In this study, we prepared an organotypic culture of avian auditory brainstem, reproducing most AIS plasticity features *in vivo*, and we revealed that activity-dependent AIS shortening occurs through the disassembly of microtubules at distal AIS via activation of CDK5/p35 signals. This study emphasizes the importance of microtubule reorganization and regulation of CDK5 activity in structural AIS plasticity and tonotopic differentiation of AIS structures in the brainstem auditory circuit.

Introduction

The axon initial segment (AIS) is a highly excitable axonal domain located near the soma and is involved in generating action potentials (Kole and Stuart, 2012). This excitable nature of AIS is attributed to its structural characteristics and the accumulation of voltage-gated Na^+ (Nav) channels, which occurs through their interaction with a scaffold protein, ankyrinG, and tethering to the submembranous actin-spectrin meshwork at AIS (Leterrier, 2018). It is now evident that the distribution of AIS, such as length and distance from the soma, shows substantial variation among neurons (Kuba, 2012) and is regulated by neural activity in a homeostatic manner (Grubb et al., 2011), thereby adjusting the membrane excitability of individual neurons.

Structural variation and homeostatic regulation of AIS have been well studied in the nucleus magnocellularis (NM) of the chicken, which is a homologue of the mammalian anteroventral cochlear nucleus. NM neurons are arranged according to their

characteristic frequency (CF) and differ in the AIS length along this tonotopic axis, with the length being shorter for higher CF, which optimizes the signal processing of the neurons in each tonotopic region (Kuba and Ohmori, 2009). In addition, the AIS of NM neurons becomes longer after cochlear damage, which maintains the integrity of auditory circuits without afferent inputs (Kuba et al., 2010). We recently revealed that activity-dependent regulation of AIS length also occurs during development; the AIS is shortened by afferent input, specifically in higher-CF neurons, creating a tonotopic difference in AIS length (Akter et al., 2020). As AIS shortening did not affect the periodicity of the submembranous meshwork or the signal intensity of AIS proteins, shortening would occur through reorganization of the distal AIS structure. Ca^{2+} entry through L-type voltage-gated Ca^{2+} (Cav) channels and the subsequent activation of calcineurin mediate AIS relocation in hippocampal neurons (Grubb and Burrone, 2010; Evans et al., 2013). However, the mechanisms linking neuronal activity by reorganizing the distal AIS structure remain elusive.

Cytoskeletons in AIS include the submembranous actin-spectrin meshwork and the cytosolic microtubule lattice (Leterrier et al., 2018). In addition, the localization of ankyrinG at the AIS is stabilized by its interaction with microtubules via end-binding proteins (EB1 and EB3) (Fréal et al., 2016) and by its tethering to the extracellular matrix via neurofascin186 (Hedstrom et al., 2007), plasma membrane via the palmitoylation (He et al., 2012), and submembranous meshwork via β4-spectrin (Dzhashiashvili et al., 2007; Yang et al., 2007). Notably, microtubules have a polarized structure and grow and shrink predominantly from one of their ends (plus-end) by regulating polymerization and depolymerization (Goodson and Jonasson, 2018). Furthermore, microtubules have a uniform orientation in the axon, with their plus-ends

facing the distal side. These features are preferable in explaining the reorganization of distal AIS structures, leading to the hypothesis that the disassembly of microtubules plays a role in AIS shortening.

Cyclin-dependent kinase 5 (CDK5) is a member of the cyclin-dependent kinase (CDK) family of serine/threonine kinases. CDK5 is ubiquitously expressed in neurons, its activity is regulated by activator proteins p35 and p39, and is involved in the microtubule reorganization (Shah and Lahiri, 2017). Moreover, activation and/or inhibition of CDK5 have been reported to affect AIS structure (Trunova et al., 2011; Evans et al., 2015; Klinman et al., 2017), suggesting its possible contribution to AIS shortening in NM neurons.

In this study, we explored the molecular mechanisms of AIS shortening using pharmacological screening and overexpression of genes in slice cultures of NM (Adachi et al., 2019). The cultured NM neurons reproduced most features of homeostatic AIS plasticity *in vivo*; an elevation of activity shortened the AIS length and lowered membrane excitability, specifically in high-CF regions, creating a tonotopic difference in AIS length. We revealed that AIS shortening occurred via destabilization of microtubules at the distal AIS because of activation of CDK5/p35, which was triggered by an elevation of $[Ca^{2+}]_i$ and subsequent activation of multiple signaling molecules.

Materials and Methods

Animals

Chickens (*Gallus domesticus*) of either sex at embryonic day 11 (E11) were used in the experiments. The care of experimental animals was in accordance with the regulations

for animal experiments at Nagoya University, and the institutional committee approved the experiments.

Organotypic slice culture

The detailed procedure has been previously described (Adachi et al., 2019). Briefly, chick embryos were anesthetized by cooling eggs in ice-cold water, and the brainstem was dissected in high-glucose artificial cerebrospinal fluid (HG-ACSF) (concentration in mM; 75 NaCl, 2.5 KCl, 26 $NaHCO_3$, 1.25 NaH_2PO_4, 1 $CaCl_2$, 3 $MgCl_2$, and 100 glucose, pH7.3) bubbled with 95% O_2 and 5% CO_2. Four to five coronal slices (200 μm) were obtained using a vibratome (VT1200, Leica) (Fig. 1A–C). Slices containing high- or low-CF NM regions were collected, transferred onto a Millicell membrane insert (Millipore) in a culture dish (35 mm), and cultured for 10 d *in vitro* (DIV) in Neurobasal medium (Life Technologies) containing 2% B-27 serum-free supplement (Life Technologies), 1 mM glutamate solution (Life Technologies), and 1% penicillin-streptomycin solution (Wako). During the first 4 d, 5% fetal bovine serum (Biowest) was added, and half of the medium was changed twice a week. NM neurons were depolarized for 3 d from 7DIV by adding KCl to the medium unless otherwise stated.

Pharmacology

All pharmacological experiments were performed at 7DIV unless otherwise stated. Following reagents were used: DNQX, 8-Br-cAMP, nimodipine, 2-APB, KT5720, Rp-cAMPS, W13, doxycycline hyclate, taxol (paclitaxel), and nocodazole (Sigma); D-AP5 and ryanodine (Alomone); TTX and cyclosporin A (Wako); MTEP hydrochloride and LY367385 (Tocris); ω-conotoxin GVIA and ω-agatoxin IVA (Peptide Institute); TTA-

147 P2 (Merck); (S)-(–)-Bay-K-8644, AZD6244, and PD98059 (Cayman); forskolin, PMA,
148 GF109203X, TATCN21, roscovitine, okadaic acid, U0126, and jasplakinolide
149 (Calbiochem); taccalonolide AJ and tubacin (MedChemExpress); 4-aminopyridine
150 (Nacalai). All reagents were added to the culture medium at least 1 h before KCl
151 treatment at a concentration less than 10 times the half-maximal effective concentration.
152
153 **Immunohistochemistry**
154 NM neurons were labeled by injecting dextran (MW 3000) conjugated with TMR (Life
155 Technologies, 10–40% in 0.1 M phosphate buffer adjusted to pH 2.0 with HCl) into the
156 midline tract region of cultured slices 2 hrs before fixation. The slices were fixed with a
157 periodate-lysine-paraformaldehyde fixative (0.4% paraformaldehyde, 2.7% lysine HCl,
158 0.21% $NaIO_4$, and 2.85 mM Na_2HPO_4) for 12 min at room temperature. Non-specific
159 binding of the antibodies was reduced by incubating the slices for 4 hrs with PBS
160 containing 1% donkey serum, 0.05% carrageenan, and 0.3% Triton X-100. The primary
161 antibodies used were as follows: mouse monoclonal panNav antibody (5 μg/ml, Sigma),
162 guinea pig anti-chick polyclonal Nav1.6 antibody (0.49 μg/ml, Kuba et al., 2006),
163 Nav1.2 antibody (0.68 μg/ml, Kuba et al., 2014), rabbit polyclonal ankyrinG antibody
164 (5 μg/ml, Bouzidi et al., 2002), rabbit polyclonal TRITC (TMR) antibody (2.5 μg/ml,
165 Life Technologies), rabbit polyclonal RFP antibody (5 μg/ml, Rockland), and rabbit
166 polyclonal GFP antibody (x500, MBL). After overnight incubation with the primary
167 antibodies at room temperature, the slices were incubated with secondary antibodies
168 conjugated with Alexa (Life Technologies) for 2 hrs, mounted on a glass slide, cover-
169 slipped, and observed under a confocal laser-scanning microscope (FV1000, Olympus)
170 with a ×40, 0.9-NA objective (Olympus). Serial sections were Z-stacked at a step of 0.8

μm. The distance from the soma and length of the AIS were measured as previously described (Akter et al., 2020). For the quantification of signal intensity, images were captured using the same microscope settings. Intensity profiles were created by measuring the signals along the axons within 50 μm of the soma. The background signal was subtracted.

Electrophysiology

A patch-clamp recording was also performed. The cultures were perfused with an ACSF (concentration in mM; 125 NaCl, 2.5 KCl, 26 $NaHCO_3$, 1.25 NaH_2PO_4, 2 $CaCl_2$, 1 $MgCl_2$, and 17 glucose, pH 7.3) when spikes were recorded under whole-cell or cell-attached mode. When sodium current was recorded, $[Na^+]_o$ was decreased to 27.3 mM by isotonic replacement of Na^+ with TEA^+ (tetraethylammonium) for whole-cell mode (E_{Na} = +25.8 mV) but not for outside-out mode (E_{Na} = +69.8 mV), whereas $[Ca^{2+}]_o$ was decreased to 0.5 mM, and 4-aminopyridine (0.2 mM), Cs^+ (5 mM), $CdCl_2$ (0.2 mM), $NiCl_2$ (0.5 mM), SR95531 (10 μM), and DNQX (20 μM) were added for both modes. The pipettes were filled with a K^+-based solution (concentration in mM; 113 K-gluconate, 4.5 $MgCl_2$, 0.1 EGTA, 14 $Tris_2$-phosphocreatine, 4 Na_2-ATP, 0.3 Tris-GTP, 9 HEPES-KOH, pH 7.2) for spike recording and a Cs^+-based solution (concentration in mM; 150 CsCl, 10 NaCl, 0.2 EGTA, and 10 HEPES-CsOH, pH7.2) for sodium current recording. The electrode capacitance and series resistance (3–7 MΩ) were electronically compensated by up to 70%. The recording temperatures were 37–38 °C for the current clamp and 20 °C for the voltage clamp. The liquid junction potential (3.1–8.0 mV) was corrected after the experiments. The data were sampled at 100 kHz and low-pass filtered at 10 kHz.

Spikes were recorded without holding current by applying current pulses at intervals of 1–2 s in increments of 40 pA. The threshold current was defined as the minimum current required for spike generation and the threshold voltage as the voltage corresponding to an inflection point in the time derivative just above the threshold current. The steady-state inactivation curve of the sodium current was fitted to the Boltzmann equation: $I/I\mathrm{max} = 1/\{1 + \exp[-(V_m - V_{1/2})/S]\}$, where I is the tail current amplitude, Imax is the maximum tail current amplitude, V_m is the membrane potential, $V_{1/2}$ is the half-inactivation voltage, and S is the slope factor (Kuba and Ohmoril, 2009; Akter et al., 2020).

Plasmid construction

The following plasmids were used: phSyn1-TetOn3G-WPRE, pTRE3G-tdTomato-WPRE, pTRE3G-tdTomato-P2A-dnCDK5-WPRE, pTRE3G-tdTomato-P2A-p35-WPRE, pTRE3G-tdTomato-P2A-p35(T138A)-WPRE, pTRE3G-tdTomato-P2A-CDK5-WPRE, and pTRE3G-mGreenLantern-P2A-CDK5-WPRE. All plasmids were constructed by inserting the following sequences into the plasmid backbone of pCAG-floxedSTOP-tdTomato-WPRE (Egawa and Yawo, 2019) using In-Fusion cloning (TaKaRa); hSyn1 promoter (pLenti Syn hChR2-EYFP-Nav1.2II-III: a gift from Matthew S. Grubb) (Grubb and Burrone, 2010), TetOn3G and TRE3GS promoter (pTetOne Vector: Clontech # 634301), mGreenLantern (LifeAct-mGreenLantern: addgene plasmid # 164459, a gift from Gregory Petsko) (Campbell et al., 2020), CDK5 and dominant-negative CDK5 (Cdk5-HA and Cdk5-DN-HA: addgene plasmid # 1872 and 1873, a gift from Sander van den Heuvel) (van den Heuvel and Harlow, 1993), and p35 (pCMV-P35: addgene plasmid # 1347, a gift from Li-Huei Tsai). Thr138 of p35

was replaced with Ala using PCR-based site-directed mutagenesis for p35(T138A). All constructs were verified by Sanger sequencing.

In ovo electroporation

The present procedure was slightly modified from the previous report (Egawa and Yawo, 2019). Briefly, a plasmid cocktail (0.4–0.5 μg/μl of each) was injected into the neural tube of chick embryos at E2 (HH Stage 10–12; Hamburger and Hamilton, 1951) and introduced into the right side of the hindbrain (rhombomere 3–8). Electrical pulses were applied using a pair of electrodes (CUY613P1, NEPAGENE) placed 2 mm apart in parallel. The settings of the electroporator (NEPA21, NEPAGENE) were as follows: poring pulse:15 V, 30 ms width, 50 ms interval, three pulses, 10% decay; and transfer pulse:5 V, 50 ms width, 50 ms interval, five pulses, 40% decay.

Quantitative RT-PCR

Detailed procedures have been described previously (Kuba et al., 2015). Cultures were incubated with normal or high-K^+ medium for 1 (8DIV) or 3 d (8–10DIV), and NM tissues in the high-CF region were excised using a fine needle under observation with a dissecting microscope immediately after incubation. Tissues from four animals were pooled for each set of experiments. Total RNA was extracted using a NucleoSpin RNA Plus XS kit (TaKaRa). The quality and concentration of the extracted RNA were measured with an Agilent 2100 Bioanalyzer (Agilent) and NanoDrop2000C (Thermo Fisher Scientific), and cDNA was synthesized using the PrimeScript IV cDNA synthesis kit (TaKaRa). The mRNA levels of CDK5, p35, and GAPDH were quantified using the THUNDERBIRD SYBER qPCR Mix (TOYOBO) with an Mx3005P QPCR

system (Agilent). The primers used are listed in Table. Cycle threshold data of individual molecules were analyzed using GAPDH as an internal standard, and the ratio was calculated between normal and high-K^+ media.

Statistics

The normality of data and equality of variance were evaluated using the Shapiro-Wilk test and F-test, respectively. Statistical significance was determined using a two-tailed Student's *t*-test for comparisons between the two groups. ANOVA or Kruskal-Wallis test was used for the analysis of variance, and the *post-hoc* Tukey test or Steel-Dwass test for multiple pairwise comparisons. Values are presented as the mean ± SE. The level of significance was set at $p < 0.05$.

Results

Cultured NM neurons differed in AIS length among tonotopic regions

We examined the geometry of AIS in high-CF and low-CF regions in cultured NM for 7–10DIV, corresponding to E18–21, after visualizing the axon with a retrograde tracer and labeling the AIS with a panNav antibody (Fig. 1A–C). PanNav signals could be seen on retrogradely labeled axons of cultured NM neurons (Fig. 1D). These signals were colocalized with ankyrinG signals (Fig. 1H), confirming that they represented the AIS structure. The length of the AIS was slightly shorter for the high-CF region at 7DIV, and the difference became significant by 10DIV (Fig. 1F); it was 25 μm and 27 μm at 7DIV, whereas 25 μm and 28 μm at 10DIV for the high-CF and low-CF regions, respectively. The AIS length did not change further after 10DIV during our observation until 14DIV, indicating that 7DIV would almost complete the maturation and

differentiation of the AIS. Notably, the position of the proximal end of the AIS did not differ between the tonotopic regions irrespective of days in culture, whereas that of the distal end was distributed more proximally for the high-CF region, specifically at 10DIV (Fig. 1E). AIS thickness did not differ tonotopically at the proximal end. In contrast, it was slightly thinner in the low-CF region at the distal end (Fig. 1G). The primary subtype of Nav channels at the AIS was Nav1.6, irrespective of age and tonotopic region (Fig. 1I, J). These results agree with *in vivo* observations (Akter et al., 2020).

Cultured NM neurons reproduced most features of AIS plasticity *in vivo*

NM neurons in culture show spontaneous synaptic activity in both tonotopic regions (Adachi et al., 2019). We then tested the contribution of these activities to the tonotopic differentiation of AIS length by adding DNQX (20 μM) and TTX (0.1 μM) to the medium for 3 d from 7DIV. The blockade of spontaneous activity increased the AIS length, specifically in high-CF neurons, abolishing the tonotopic difference in AIS length (Fig. 2A–D); it was 28 μm and 30 μm for high-CF and low-CF neurons, respectively. In addition, when the spontaneous activity was elevated for 3 d from 7DIV by increasing $[K^+]$ in the medium by two times (10.6 mM), the AIS length was shortened in the high-CF neurons (20 μm) but not in the low-CF neurons (31 μm) (Fig. 2F–I). Elevating activities by blocking potassium channels with 4-aminopyridine (0.5 mM) caused a similar AIS shortening in high-CF neurons (20.4±0.9 μm, n = 39). These findings confirmed that the activity-dependent reorganization of AIS occurs primarily in high-CF neurons, underlying the tonotopic differentiation of AIS length (Akter et al., 2020). Importantly, these manipulations did not affect the position of the proximal end

(Fig. 2C, H), indicating that AIS shortening occurs via cytoskeletal reorganization at the distal end. The subtype of Nav channels did not change during the manipulations either (Fig. 2E, J), which also agreed with the findings *in vivo*.

We then characterized the progression of AIS shortening during high-K^+ treatment in high-CF neurons (Fig. 2K–M). One-day treatment with a high-K^+ medium did not change the AIS length (24 μm). Furthermore, an additional 2 d incubation in a normal medium did not shorten the AIS either (26 μm), suggesting that AIS shortening would require elevation of activities for substantial periods (> 1 d). We also examined recovery from the shortening by incubating the cultures in a normal medium after 3 d treatments with a high-K^+ medium (Fig. 2N–P). The AIS returned to its original length within 3 d of incubation in the normal medium; the length was 22 μm and 27 μm for 1 and 3 d incubation, respectively, confirming the reversibility of the shortening.

We evaluated the effects of AIS shortening on the biophysical features of the high-CF neurons. We recorded the whole-cell sodium current under voltage clamp at –20 mV with a pre-pulse between −85 and −20 mV. The current amplitude was reduced by 40% in the high-K^+-treated group compared to the control, whereas the voltage dependence of inactivation did not differ between the two groups (Fig. 3A–D). These results suggest that the same subtype of Nav channels mediates the current, supporting the immunohistochemical findings (Fig. 1I, J, 2J). Importantly, we could not detect sodium current in outside-out patches from the soma in both control (13 cells) and high-K^+-treated (15 cells) groups (Fig. 3E), indicating that the reduction of whole-cell sodium current in the high-K^+-treated group would primarily reflect a decrease of axonal Nav channels because of the AIS shortening. We also recorded action potentials in response to somatic current injection under current clamp, which revealed an elevation of

threshold current, decreased amplitude, and maximum dV/dt in the high-K^+-treated group. Despite a decreasing tendency, threshold voltage did not differ significantly between the groups (Fig. 3F–K). The absence of a change in threshold voltage might be related to the rich expression of Kv1 channels in the neurons (Kuba et al., 2015), which would facilitate the underestimation of threshold voltage at the AIS when monitored at the soma (Kole and Stuart, 2008). Notably, the control neurons showed a barrage of spontaneous synaptic and spike activities without stimuli, but these activities did not occur in the high-K^+-treated neurons (Fig. 3L). As these activities were still more prominent in the control neurons under the blockade of Kv1 current with dendrotoxin (40 nM) (Fig. 3M), the results indicated that AIS shortening by high-K^+ treatment reduced sodium current and membrane excitability of neurons, thereby contributing to homeostatic control of activity in the circuit. Thus, cultured NM neurons reproduced most features of AIS plasticity *in vivo* and should be a good model for examining the molecular mechanisms of plasticity.

Ca^{2+} entry via multiple pathways mediated AIS shortening

High-K^+ treatment increases spontaneous synaptic input, which elevates $[Ca^{2+}]_i$ in cultured NM neurons via activation of glutamate receptors and/or Cav channels (Adachi et al., 2019) (Fig. 4B). We explored the triggers of AIS shortening during high-K^+ treatment using specific inhibitors of these receptors and channels in high-CF neurons (Fig. 4A–D). Inhibition of ionotropic glutamate receptors (iGluRs) with DNQX (20 μM) and AP-5 (50 μM) suppressed AIS shortening (25 μm). These receptors cause Ca^{2+} influx not only by permeating Ca^{2+} but also by activating Cav channels via depolarization. L- and T-type channels are localized preferentially at postsynaptic

membranes, whereas P/Q- and N-type Cav channels are known to locate at presynaptic as well as postsynaptic membranes (Catterall, 2000), which were consistent with the effects of specific blockers on spontaneous spikes in the culture (Fig. 4G, H) and the previous observations in the neurons (Koyano et al., 1996; Lu and Rubel, 2005). Inhibitors of these Cav channels occluded the effects of high-K^+ treatment when they were applied separately, and the effects were maximized when applied as a cocktail (Fig. 4D). The lengths were 27, 28, 28, 28, and 31 μm for inhibitors of L- (nimodipine, 10 μM), P/Q- (ω-agatoxin IVA, 0.2 μM), N- (ω-conotoxin GVIA, 2 μM), T-type (TTA-P2, 2 μM) channels, and a cocktail, respectively. In contrast, an activator of L-type Cav channels (Bay-K, 1 μM) caused AIS shortening (23 μm) in the normal medium (i.e., without high-K^+ treatment) (Fig. 4E), confirming the importance of elevation of $[Ca^{2+}]_i$ in AIS shortening.

The inhibition of group I metabotropic glutamate receptors (mGluRs) with MTEP (50 nM) and LY367385 (20 μM) also reduced the effects of high-K^+ treatment (26 μm) (Fig. 4D). In addition, inhibitors of both inositol trisphosphate (IP_3) receptors (2-APB, 50 μM) and ryanodine receptors (ryanodine, 50 μM) showed similar effects, with a length of 28 μm and 28 μm, respectively (Fig. 4F). These results are supported by the expression of group I mGluRs in neurons (Zirpel et al., 2000) and may emphasize the importance of $[Ca^{2+}]_i$ elevation in AIS shortening.

Intracellular signals of AIS shortening

We explored intracellular signals of AIS shortening downstream of Ca^{2+} by testing the effects of kinase inhibitors during high-K^+ treatment in the culture (Fig. 5A, B). To our surprise, AIS shortening was sensitive to multiple kinase inhibitors (Fig. 5C, D), with a

length of 26 μm with KT5720 (0.5 μM), 28 μm with Rp-cAMPS (100 μM) for protein kinase A (PKA), 29 μm with GF109203X (50 nM) for protein kinase C (PKC), and 30 μm with TATCN21 (5 μM) for calmodulin-dependent kinase II (CaMKII), suggesting substantial crosstalk among the kinases. However, AIS shortening was less sensitive to phosphatase inhibitors; the length was 22 μm with okadaic acid (20 nM) for PP1/PP2A, and 26 μm with cyclosporin A (50 nM) for PP2B (Fig. 5F). PKA and CaMKII were activated via calmodulin (CaM) in a Ca^{2+}-dependent manner (Xia and Storm, 2005). Consistently, inhibition of CaM with W13 (50 μM) blocked the effects of high-K^+ treatment (26 μm) (Fig. 5D). Moreover, activation of either PKA or PKC alone mimicked the effects of high-K^+ treatment (Fig. 5C, G); the AIS length was 21 μm for forskolin (10 μM, adenylate cyclase activator) and 21 μm for PMA (0.5 μM, PKC activator). These results confirmed the involvement of PKA/PKC/CaMKII in AIS shortening.

These kinases can activate the extracellular signal-regulated kinase (ERK1/2) pathway in neurons (Miningou and Blackwell, 2020), and ERK1/2 is known as an upstream molecule of CDK5 (Shah and Lahiri, 2017). Thus, we hypothesized that ERK1/2 integrates PKA/PKC/CaMKII signals and mediates AIS shortening via CDK5 activation. Inhibition of either mitogen-activated protein kinase kinase (MEK1/2) or CDK5 suppressed AIS shortening during the high-K^+ treatment (Fig. 5C, D), with a length of 28 μm with AZD6244 (10 μM) for MEK1/2 and 28 μm with roscovitine (2 μM) for CDK5. Other MEK1/2 inhibitors showed similar dose-dependent effects (Fig. 5D, E); the length was 23 μm (0.5 μM), 25 μm (2 μM), and 27 μm (20 μM) with U0126, and 28 μm with PD98059 (100 μM). More importantly, these inhibitors occluded AIS shortening during the activation of either PKA or PKC (Fig. 5C, H); the

lengths were 24 μm and 30 μm for AZD6244 and roscovitine, respectively, in the presence of forskolin, and 27 μm and 27 μm in the presence of PMA. These results support the hypothesis that ERK1/2 and CDK5 contribute to the shortening of AIS downstream of PKA/PKC/CaMKII in NM neurons.

Activation of CDK5 was required for AIS shortening

To confirm the involvement of CDK5 in AIS shortening, we introduced dominant-negative CDK5 (dnCDK5) in right-sided NM neurons by *in ovo* electroporation at E2 and overexpressed the genes under Tet-On control in high-CF regions in the culture, whereas doxycycline (DOX, 2 μM) was added for 4 d in the high-K^+ medium (Fig. 6A, B). The overexpression of dnCDK5 occluded the AIS shortening during the high-K^+ treatment with little changes in the maximum intensity of panNav signals at the AIS (Fig. 6C, D, L); the length was 28 μm in dnCDK5-positive neurons, whereas it was 24 μm for neurons in the opposite (non-electroporated) side and 22 μm for those expressing tdTomato alone.

Overexpression of CDK5 did not affect the AIS length (28 μm), whereas overexpression of p35 caused AIS shortening (23 μm) in normal medium (Fig. 6E–H, M). Notably, a mutation in the phosphorylation site of p35(T138A) occluded AIS shortening (30 μm) (Fig. 6I, J, M). In addition, overexpression of p35 and CDK5 eliminated AIS (34 of 34 cells) (Fig. 6K, M), suggesting the importance of CDK5/p35 activity in regulating AIS length in the high-CF neurons. In contrast, in low-CF neurons, overexpression of p35 did not affect AIS length (Fig. 6O); the lengths were 28 μm and 30 μm for control and overexpression of p35, respectively, indicating that molecules downstream of CDK5 would differ between high- and low-CF neurons and are

411 responsible for the tonotopic difference in the AIS length in NM. As high-K^+ treatment
412 did not affect the mRNA levels of CDK5 and p35 in NM (Fig. 6N), posttranscriptional
413 regulation of these molecules might be involved in the process.
414
415 **Microtubule reorganization contributed to AIS shortening**
416 Microtubules contribute to the assembly of AIS structures by anchoring ankyrinG via
417 EB1 and EB3 (Leterrier et al., 2011; Fréal et al., 2016). Thus, we tested the possibility
418 that CDK5 mediates AIS shortening via the disassembly of microtubules. We incubated
419 the cultures with microtubule-stabilizing agents, taxol (50 nM), and taccalonolide AJ
420 (50 nM), and found that these microtubule stabilizers suppressed the AIS shortening
421 during the high-K^+ treatment in the high-CF neurons (Fig. 7A–D); the AIS length was
422 27 μm with taxol and 28 μm with taccalonolide AJ. AIS shortening was also occluded
423 (25 μm) by tubacin (0.1 μM), an inhibitor of HDAC6, an enzyme that destabilizes
424 microtubules via deacetylation of tubulin. In addition, taxol occluded AIS shortening by
425 overexpression of p35 (29 μm) (Fig. 7F, G, I left) or by the activators of PKA (28 μm)
426 or PKC (29 μm) (Fig. 7D right). Notably, taxol occluded the elimination of AIS after
427 the overexpression of p35 together with CDK5 (22 μm) (Fig. 7F, H, I right), consistent
428 with the idea that the elimination was attributed to the facilitation of AIS shortening
429 rather than the toxicity of strong CDK5/p35 signals. Moreover, the inhibition of
430 PP1/PP2A by okadaic acid, which promotes phosphorylation of p35 at T138 (Kamei et
431 al., 2007), shortened AIS (22 μm), and this AIS shortening was suppressed by taxol (29
432 μm) (Fig. 7B, E), suggesting that phosphorylation of p35 at T138 underlies AIS
433 shortening via interaction with microtubules. We also treated the cultures with a
434 microtubule destabilizing agent, nocodazole (10 μM), which completely eliminated

AIS, confirming the importance of microtubule integrity in maintaining AIS structure. In contrast, jasplakinolide, which promotes actin polymerization and stabilization, did not occlude (22 μm) AIS shortening in the high-K^+ medium (Fig 7C, D left).

Discussion

In the slice culture of NM, AIS shortening occurred in high-CF neurons but not in low-CF neurons during high-K^+ treatment, creating a tonotopic difference in AIS length, as observed *in vivo* (Kuba and Ohmori, 2009). As spontaneous synaptic activity and Ca^{2+} influx did not differ between the neurons during high-K^+ treatment (Adachi et al., 2019), the results implied that the ability of AIS plasticity is determined intrinsically in a cell-specific manner and is equipped explicitly in high-CF neurons (Akter et al., 2020). The cell-type specificity of AIS plasticity has also been reported in other brain regions, such as the olfactory bulb, sensory cortex, and hippocampus (Grubb and Burrone, 2010; Gutzmann et al., 2014; Chand et al., 2015). AIS shortening progressed over time in the order of days via reorganization of the distal AIS structure, which reduced the membrane excitability of neurons, suggesting its involvement in homeostatic control of neural activity. Thus, structural AIS plasticity in cultured NM neurons reproduces most features of AIS plasticity *in vivo* (Kuba et al., 2010). With accessibility to pharmacological and genetic manipulations, slice culture of NM would be a powerful tool for exploring the molecular mechanisms of AIS plasticity.

Ca^{2+} pathways of AIS plasticity

Relocation of AIS occurs via Ca^{2+} entry through L-type Cav channels in dissociated neurons from the hippocampus and olfactory bulb (Grubb and Burrone, 2010; Evans et

al., 2013; Chand et al., 2015). Because these Cav channels are preferentially localized in somatodendritic domains (Catterall, 2000), these findings suggest the contribution of global $[Ca^{2+}]_i$ within neurons to AIS plasticity. However, AIS shortening in NM neurons occurs via multiple Ca^{2+} pathways, such as Ca^{2+} entry through several types of Cav channels and glutamate receptors, and Ca^{2+} release from Ca^{2+} stores, confirming the importance of global $[Ca^{2+}]_i$ elevation within neurons for AIS shortening. The variation in Ca^{2+} pathways among studies might be related to differences in the characteristics of neurons (i.e., composition of channels and receptors), phenotype of AIS plasticity (relocation vs. shortening), and/or preparation (dissociated vs. organ culture). The present observations also suggested a possibility that local $[Ca^{2+}]_i$ at the AIS is involved in the AIS shortening, as P/Q-, N-, and T-type Cav channels are known to localize at the AIS (Bender and Trussell, 2009; Yu et al., 2010), while cisterna organelle, a Ca^{2+} store at the AIS, is coupled with T-type Cav channels and elevates $[Ca^{2+}]_i$ at the AIS (Lipkin et al., 2021).

The AIS length roughly correlated with the level of activity and/or depolarization in the cultured NM neurons; it became shorter during high-K^+ treatment and longer in the presence of DNQX and TTX (Fig. 2), which agreed with our previous observations *in vivo* (Kuba et al., 2010). This may indicate that the AIS length is determined by $[Ca^{2+}]_i$; the length is longer for lower $[Ca^{2+}]_i$. Blockade of the single Ca^{2+} pathway occluded AIS shortening and even elongated AIS, whereas blockade of multiple Ca^{2+} pathways showed only a minor additional effect. These results may indicate that the machinery of AIS shortening has a steep relationship with $[Ca^{2+}]_i$; it is highly sensitive to $[Ca^{2+}]_i$ and is easily saturated with a slight change in $[Ca^{2+}]_i$. This idea is compatible with our previous observation that $[Ca^{2+}]_i$ was elevated to only ~200 nM by depolarization

corresponding to that during the high-K^+ treatment (Adachi et al., 2019). Of note, 1-d treatment with the high-K^+ medium did not cause AIS shortening even 3 d after the treatment. These results indicate that long-lasting changes in basal Ca^{2+} levels are required for structural AIS changes, which are preferable for the homeostatic control of neural activity in a circuit.

Multiple signaling pathways of AIS plasticity

One surprising finding of this study was that multiple kinase inhibitors occluded AIS shortening. Although these inhibitors are known to affect molecules other than the target at higher concentrations (Bain et al., 2003), we do not think that the results were attributable to the non-specific effects of these drugs for the following reasons. First, the effects depended on the drug concentration, and the concentration of inhibitors was kept as low as possible during the experiments (see Methods). Second, multiple inhibitors could reproduce the effects of specific molecules. Third, activators caused the opposite effects. Thus, the present results would indicate multiple pathways for AIS shortening and strong crosstalk among these pathways while converging on ERK1/2 and CDK5. Although major signals in physiological schemes still need to be determined, the presence of multiple pathways and their crosstalk would be advantageous in reliably inducing AIS reorganization and adjusting activity at an appropriate level in various situations.

Roles of CDK5 in AIS plasticity

Several signaling molecules have been reported to regulate AIS structure and/or protein localization. Among them, formin2, GSK3β, and pMLC are known to affect AIS length,

and their inhibition causes the shortening of AIS (Tapia et al., 2013; Berger et al., 2018; Zhang et al., 2021). Importantly, however, the AIS shortening during inhibition of these molecules resulted from the uniform reduction of ankyrinG signals along the AIS and progressed rather rapidly (within hours). In contrast, AIS shortening in NM occurs without changes in the signal intensity of AIS proteins and requires much longer periods (a few days). These results indicate that the reorganization of AIS structure in NM is restricted to the distal part of AIS and includes rate-limiting steps, suggesting the involvement of different mechanisms in the process.

We found that CDK5 activation is critical for inducing AIS shortening in NM. Overexpression of CDK5 alone did not shorten AIS, whereas overexpression of p35 caused substantial AIS shortening in the culture. This is compatible with reports that ERK1/2 can upregulate both CDK5 and p35, but CDK5 is ubiquitously expressed, and its activity is primarily regulated by the level of p35 expression (Shah and Lahiri, 2014). It is important to note that activation of CDK5 promoted AIS shortening to a different extent among tonotopic regions, with the effects being more prominent in high-CF neurons, which would underlie the tonotopic difference in AIS length in NM. In addition, the effects of CDK5 on AIS length were opposite in previous reports; in the Drosophila mushroom body, activation of CDK5 increased the length of AIS-like structures (Trunova et al., 2011), whereas inhibition of CDK5 decreased the AIS length in dissociated hippocampal neurons (Evans et al., 2015; Klinman et al., 2017). What then underlies the variation in CDK5-mediated effects on AIS length among neurons? AIS length decreases because of reorganization of the distal AIS structure in NM (Akter et al., 2020), and CDK5 mediates this process via the disassembly of microtubules (Fig. 7). CDK5/p35 may regulate microtubule remodeling in pleiotropic manner depending

on autophosphorylation (Shah and Lahiri, 2017). CDK5 phosphorylates p35 at S8, allowing its translocation from the plasma membrane and interaction with microtubules for microtubule polymerization (Asada et al., 2012; Hou et al., 2007). However, CDK5 also phosphorylates p35 at T138, preventing this interaction and inhibiting microtubule polymerization (He et al., 2008), while T138 is dephosphorylated by phosphatases, PP1 and PP2A (Kamei et al., 2007), which agreed with the positive and negative effects on the AIS shortening by okadaic acid and p35(T138A), respectively, in high-CF NM neurons (Fig. 6, 7). Therefore, one possible explanation for the discrepancy in CDK5-mediated effects is that the levels of these phosphatases differ among neurons, being lower in NM neurons, suppressing microtubule polymerization and facilitating AIS shortening. Importantly, substrates of CDK5 include those that regulate microtubule organization, either positively or negatively. For example, phosphorylation of doublecortin at S297 negatively regulates its microtubule-binding affinity, promoting the depolymerization of microtubules (Tanaka et al., 2004). In contrast, phosphorylation of ndel1 facilitates dynein-mediated retrograde transport and promotes the polarization of microtubules, leading to elongation of the AIS (Klinman et al., 2017). Thus, another possible explanation is that CDK5 is differentially coupled with its substrates in individual neurons, creating cell-specific effects of CDK5 on AIS length. We found that inhibition of HDAC6 by tubacin occluded AIS shortening (Fig. 7). HDAC6 interacts with EB1 (Zilberman et al., 2009), which mediates both capping of microtubule plus ends and association of ankyrinG with microtubules at the AIS (Leterrier et al., 2011; Fréal et al., 2016). Moreover, HDAC6 interferes with forming AIS via the hyperacetylation of tubulins (Tapia et al., 2010). Therefore, it is important to determine whether HDAC6 is involved in AIS shortening downstream of CDK5 in NM.

555

556 **References**

557 Adachi R, Yamada R, Kuba H. (2019) Tonotopic differentiation of coupling between
558 Ca^{2+} and Kv1.1 expression in brainstem auditory circuit. iScience 13: 199–213.

559 Akter N, Fukaya R, Adachi R, Kawabe H, Kuba H. (2020) Structural and functional
560 refinement of the axon initial segment in avian cochlear nucleus during development.
561 J Neurosci. 40: 6709–6721.

562 Asada A, Saito T, Hisanaga S. (2012) Phosphorylation of p35 and p39 by Cdk5
563 determines the subcellular location of the holokinase in a phosphorylation-site-
564 specific manner. J Cell Sci 125: 3421–3429.

565 Bain J, McLauchlan H, Elliott M, Cohen P. (2003) The specificities of protein kinase
566 inhibitors: an update. Biochem. J 371: 199–204.

567 Bender KJ, Trussell LO. (2009) Axon initial segment Ca^{2+} channels influence action
568 potential generation and timing. Neuron 61: 259–271.

569 Berger SL, Leo-Macias A, Yuen S, Khatri L, Pfennig S, Zhang Y, Agullo-Pascual E,
570 Caillol G, Zhu M, Rothenberg E, Melendez-Vasquez CV, Delmar M, Leterrier C,
571 Salzer JL. (2018) Localized myosin II activity regulates assembly and plasticity of
572 the axon initial segment. Neuron 97: 555–570.

573 Bouzidi M, Tricaud N, Giraud P, Kordeli E, Caillol G, Deleuze C, Couraud F, Alcaraz
574 G. (2002) Interaction of the Nav1.2a subunit of the voltage-dependent sodium
575 channel with nodal ankyrinG. In vitro mapping of the interacting domains and
576 association in synaptosomes. J Biol Chem 277: 28996–29004.

577 Campbell BC, Nabel EM, Murdock MH, Lao-Peregrin C, Tsoulfas P, Blackmore MG,
578 Lee FS, Liston C, Morishita H, Petsko GA. (2020) mGreenLantern: a bright

579 monomeric fluorescent protein with rapid expression and cell filling properties for
580 neuronal imaging. Proc Natl Acad Sci USA 117: 30710–30721.
581 Catterall WA. (2000) Structure and regulation of voltage-gated Ca^{2+} channels. Annu
582 Rev Cell Dev Biol 16: 521–555.
583 Chand AN, Galliano E, Chesters RA, Grubb MS. (2015) A distinct subtype of
584 dopaminergic interneuron displays inverted structural plasticity at the axon initial
585 segment. J Neurosci 35: 1573–1590.
586 Dzhashiashvili Y, Zhang Y, Galinska J, Lam I, Grumet M, Salzer J. (2007) Nodes of
587 Ranvier and axon initial segments are ankyrin G-dependent domains that assemble
588 by distinct mechanisms. J Cell Biol 177: 857–870.
589 Egawa R, Yawo H. (2019) Analysis of neuro-neuronal synapses using embryonic chick
590 ciliary ganglion via single-axon tracing, electrophysiology, and optogenetic
591 techniques. Curr Protoc Neurosci 87, e64.
592 Evans MD, Sammons RP, Lebron S, Dumitrescu AS, Watkins TBK, Uebele VN,
593 Renger JJ, Grubb MS. (2013) Calcineurin signaling mediates axtivity-dependent
594 relocation of the axon initial segment. J Neurosci 33: 6950–6963.
595 Evans MD, Dumitrescu AS, Kruijssen DLH, Taylor SE, Grubb MS. (2015) Rapid
596 modulation of axon initial segment length influences repetitive spike firing. Cell
597 Reports 13: 1233–1245.
598 Fréal A, Fassier C, Le Bras B, Bullie E, De Gois S, Hazan J, Hoogenraad CC, Couraud
599 F. (2016) Cooperative interactions between 480 kDa ankyrin-G and EB proteins
600 assemble the axon initial segment. J Neurosci 36: 4421–4433.
601 Goodson HV, Jonasson EM. (2018) Microtubules and microtubule-associated proteins.
602 Cold Spring Harb Perspect Biol 10: a022608.

603 Grubb MS, Burrone J. (2010) Activity-dependent relocation of the axon initial segment
604 fine-tunes neuronal excitability. Nature 465: 1070–1074.
605 Grubb MS, Shu Y, Kuba H, Rasband MN, Wimmer VC, Bender KJ. (2011) Short- and
606 long-term plasticity at the axon initial segment. J Neurosci 31: 16049–16055.
607 Gutzmann A, Ergül N, Grossmann R, Schultz C, Wahle P, Engelhardt M. (2014) A
608 period of structural plasticity at the axon initial segment in developing visual cortex.
609 Front Neuroanat 8: 11.
610 Hamburger V, Hamilton HL. (1951) A series of normal stages in the development of the
611 chick embryo. J Morphol 88: 49–92.
612 He L, Hou Z, Qi RZ. (2008) Calmodulin binding and cdk5 phosphorylation of p35
613 regulate its effect on microtubules. J Biol Chem 283: 13252–13260.
614 He M, Jenkins P, Bennett V. (2012) Cysteine 70 of ankyrin-G is *s*-palmitoylated and is
615 required for function of ankyrin-G in membrane domain assembly. J Biol Chem 287:
616 43995–44005.
617 Hedstrom KL, Xu X, Ogawa Y, Frischknecht R, Seidenbecher CI, Shrager P, Rasband
618 MN. (2007) Neurofascin assembles a specialized extracellular matrix at the axon
619 initial segment. J Cell Biol 178: 875–886.
620 Hou Z, Li Q, He L, Lim HY, Fu X, Cheung NS, Qi DX, Qi RZ (2007) Microtubule
621 association of the neuronal p35 activator of Cdk5. J Biol Chem 282: 18666–18670.
622 Kamei H, Saito T, Ozawa M, Fujita Y, Asada A, Bibb JA, Saido TC, Sorimachi H,
623 Hisanaga S. (2007) Suppression of calpain-dependent cleavage of the CDK5
624 activator p35 to p25 by site-specific phosphorylation. J Biol Chem 282: 1687–1694.

625 Klinman E, Tokito M, Holzbaur ELF. (2017) CDK5-dependent activation of dynein in
626 the axon initial segment regulates polarized cargo transport in neurons. Traffic 18:
627 808–824.
628 Kole MHP, Stuart GJ. (2008) Is action potential threshold lowest in the axon? Nat
629 Neurosci 11: 1253–1255.
630 Kole MHP, Stuart GJ. (2012) Signal processing in the axon initial segment. Neuron 73:
631 235–247.
632 Koyano K, Funabiki K, Ohmori H. **(**1996) Voltage-gated ionic currents and their roles
633 in timing coding in auditory neurons of the nucleus magnocellularis of the chick.
634 Neurosci Res 26: 29–45.
635 Kuba H. (2012) Structural tuning and plasticity of the axon initial segment in auditory
636 neurons. J Physiol 590: 5571–5579.
637 Kuba H, Ohmori H. (2009) Roles of axonal sodium channels in precise auditory time
638 coding at nucleus magnocellularis of the chick. J Physiol 587: 87–100.
639 Kuba H, Ishii TM, Ohmori H. (2006) Axonal site of spike initiation enhances auditory
640 coincidence detection. Nature 444: 1069–1072.
641 Kuba H, Oichi Y, Ohmori H. (2010) Presynaptic activity regulates Na^+ channel
642 distribution at the axon initial segment. Nature 465: 1075–1079.
643 Kuba H, Adachi R, Ohmori H. (2014) Activity-dependent and activity-independent
644 development of the axon initial segment. J Neurosci 34: 3443–3453.
645 Kuba H, Yamada R, Ishiguro G, Adachi R. (2015) Redistribution of Kv1 and Kv7
646 enhances neuronal excitability during structural axon initial segment plasticity. Nat
647 Commun 6: 8815.

Leterrier C. (2018) The axon initial segment: an updated viewpoint. J Neurosci 38: 2135–2145.

Leterrier C, Vacher H, Fache M, d'Ortoli SA, Castets F, Autillo-Touati A, Dargent B. (2011) End-binding proteins EB3 and EB1 link microtubules to ankyrin G in the axon initial segment. Proc Natl Acad Sci USA 108: 8826–8831.

Lipkin AM, Cunniff MM, Spratt PWE, Lemke SM, Bender KJ. (2021) Functional microstructure of Ca_v-mediated calcium signaling in the axon initial segment. J Neurosci 41: 3764–3776.

Lu Y, Rubel EW. (2005) Activation of metabotropic glutamate receptors inhibits high-voltage-gated calcium channel currents of chicken nucleus magnocellularis neurons. J Neurophysiol 93: 1418–1428.

Miningou N, Blackwell KT. (2020) The road to ERK activation: do neurons take alternate routes? Cell Signal 68: 109541.

Shah K, Lahiri DK. (2014) Cdk5 activity in the brain – multiple paths of regulation. J Cell Sci. 127, 2391–2400.

Shah K, Lahiri DK. (2017) A tale of the good and bad: remodeling of the microtubule network in the brain by cdk5. Mol Neurobiol 54: 2255–2268.

Tanaka T, Serneo FF, Tseng HC, Kulkarni AB, Tsai LH, Gleeson JG. (2004) Cdk5 phosphorylation of doublecortin Ser297 regulates its effect on neuronal migration. Neuron 41: 215–227.

Tapia M, Wandosell F, Garrido JJ. (2010) Impaired function of HDAC6 slows down axonal growth and interferes with axon initial segment development. PLOS One 5: e12908.

671 Tapia M, Del Puerto A, Puime A, Sánchez-Ponce D, Fronzaroli-Molinieres L, Pallas-
672 Bazarra N, Carlier E, Giraud P, Debanne D, Wandosell F, Garrido JJ. (2013) GSK3
673 and β-catenin determines functional expression of sodium channels at the axon initial
674 segment. Cell Mol Life Sci 70: 105–120.
675 Trunova S, Baek B, Giniger E (2011). Cdk5 regulates the size of an axon initial
676 segment-like compartment in mushroom body neurons of the *Drosophila* central
677 brain. J Neurosci 31: 10451–10462.
678 van den Heuvel S. Harlow E. (1993) Distinct roles for cyclin-dependent kinases in cell
679 cycle control. Science 262: 2050–2054.
680 Xia Z, Storm DR. (2005) The role of calmodulin as a signal integrator for synaptic
681 plasticity. Nat Rev Neurosci 6: 267–276.
682 Yang Y, Ogawa Y, Hedstrom KL, Rasband MN. (2007) βIV spectrin is recruited to
683 axon initial segments and nodes of Ranvier by ankyrinG. J Cell Biol 176: 509–519.
684 Yu Y, Maureira C, Liu X, McCormick D. (2010) P/Q and N channels control baseline
685 and spike-triggered calcium levels in neocortical axons and synaptic boutons. J
686 Neurosci 30: 11858–11869.
687 Zhang W, Ciorraga M, Mendez P, Retana D, Boumedine-Guignon N, Achón B, Russier
688 M, Debanne D, Garrido JJ. (2021) Formin activity and mDia1 contribute to maintain
689 axon initial segment composition and structure. Mol Neurobiol
690 https://doi.org/10.1007/s12035-021-02531-6
691 Zilberman Y, Ballestrem C, Carramusa L, Mazitschek R, Khochbin S, Bershadsky A.
692 (2009) Regulation of microtubule dynamics by inhibition of the tubulin deacetylase
693 HDAC6. J Cell Sci 122: 3531–3541.

694 Zirpel L, Janowiak MA, Taylor DA, Parks TN. (2000) Developmental changes in
695 metabotropic glutamate receptor-mediated calcium homeostasis. J Comp Neurol 421:
696 95–106.

697

698 **Table**

699 **Table 1 Primer sets used in this study**

700 CDK5

701 fwd: 5'-TGAAGGAGCTGAAGCACAAA-3' rev: 5'-CACGATCTCAGGGTCCAGAT-3'

702 p35

703 fwd: 5'-GCCAAGAAGAAGAGCTCCAA-3' rev: 5'-GGAGAGCGACTTCTTCAGGTT-3'

704 GAPDH

705 fwd: 5'-CATCCAAGGAGTGAGCCAAG-3' rev: 5'-TGGAGGAAGAAATTGGAGGA-3'

706

707 **Figure Legends**

708 **Figure 1 Structural differentiation of AIS in slice culture**

709 **A**, Development of an avian auditory system *in vivo* and *in vitro*. **B**, Brainstem auditory
710 circuit of chickens. AN, Auditory nerve; NL, Nucleus laminaris. **C**, NM is tonotopically
711 organized along the rostromedial-caudolateral axis (left). In most rostral and caudal
712 slices, NM was defined as high-CF (HCF) and low-CF (LCF) regions, respectively. NM
713 neurons were retrogradely labeled with dextran TMR (right, dotted line). R, rostral; L,
714 lateral; D, dorsal; M, medial. **D**, AIS immunostained with panNav antibody (green,
715 arrowheads) after visualizing NM neurons (TMR, magenta) for HCF and LCF at 7DIV
716 and 10DIV. **E**, Position of the proximal and distal ends of the AIS. **F, G**, Length (**F**) and
717 widths at the proximal and distal ends of AIS (**G**). Values from individual cells are

718 plotted (open circles) in this and the subsequent figures. **H**, Double immunostaining of
719 panNav and ankyrinG. Intensity profiles of panNav and ankyrinG signals along the
720 axon are shown. **I, J**, Immunostaining of Nav1.2 (**I**) and Nav1.6 (**J**). Numbers in
721 parentheses indicate the number of cells. * $p < 0.05$, ** $p < 0.01$ between tonotopic
722 regions by Kruskal-Wallis test, ## $p < 0.01$ between proximal and distal ends by
723 Student's *t*-test.
724
725 **Figure 2 Activity-dependent AIS shortening in high-CF region**
726 **A–E**, Synaptic and spike activity was blocked by DNQX/TTX for 7–10DIV. Time
727 course of experiment (**A**), AIS (green) of NM neurons (magenta) (**B**), position of
728 proximal and distal ends (**C**), length (**D**) of AIS, and immunostaining of panNav and
729 ankyrinG, Nav1.2, and Nav1.6 (**E**) for the HCF and LCF at 10DIV. **F–J**, Membrane was
730 depolarized by increasing $[K^+]_o$ in the culture medium by two times (10.6 mM, 2x$[K^+]$
731 medium) for 7–10DIV. Time course of experiments (**F**), AIS of NM neurons (**G**),
732 position of proximal and distal ends (**H**), length (**I**) of AIS, and immunostaining of
733 panNav and ankyrinG, Nav1.2, and Nav1.6 (**J**) for HCF and LCF at 10DIV. AIS length
734 for the normal (1x$[K^+]$) medium (light gray) is from Fig. 1F (10DIV). **K–M**, HCF slices
735 were cultured in 2x$[K^+]$ medium for 1 d (7–8DIV). Time course of experiments (**K**),
736 AIS of NM neurons after 2x$[K^+]$ treatment without (upper) or with (lower) subsequent
737 incubation in 1x$[K^+]$ medium for 2 d (**L**), and AIS length (**M**). **N–P**, HCF slices were
738 incubated in 1x$[K^+]$ medium for 1 or 3 d after 2x$[K^+]$ treatment for 7–10DIV. Time
739 course of the experiment (**N**), AIS of NM neurons at 1 d (upper) and 3 d (lower) after
740 2x$[K^+]$ treatment (**O**), and AIS length (**P**). The AIS length for the 2x$[K^+]$ medium
741 (green) is from Fig. 2I. Numbers in parentheses indicate the number of cells.

742 Arrowheads indicate the AIS. ** $p < 0.01$ compared with control by Kruskal-Wallis test
743 (**D**, **I**), between tonotopic regions by Student's *t*-test (**H**). * $p < 0.05$, ** $p < 0.01$ by one-
744 way ANOVA and *post-hoc* test (**M**, **P**).
745
746 **Figure 3 AIS shortening reduced sodium current and membrane excitability**
747 **A**, Time course of the experiments. HCF slices were cultured in 2x[K^+] medium for 7–
748 10DIV, and whole-cell recordings were made at 10DIV. **B**, Whole-cell sodium currents
749 were recorded at –20 mV with a pre-pulse (30 ms) from –85 mV to –20 mV. Control
750 (left) and 2x[K^+] (right). **C**, Voltage dependence of inactivation. Values were fitted to
751 the Boltzmann equation, and $V_{1/2}$ was specified. **D**, Amplitude of sodium current. **E**,
752 Outside-out sodium currents were not detected at –30 mV with a pre-pulse (30 ms) from
753 –85 mV to –20 mV. Control (left) and 2x[K^+] (right). Membrane capacitance was
754 13.3±1.1 pF (n = 10) and 13.8±1.4 pF (n = 7) for whole-cell membrane from control
755 and 2x[K^+], respectively (p = 0.73), whereas 2.4±0.5 pF (n = 13) and 2.1±0.3 pF (n =
756 15) for outside-out patches (p = 0.56). **F**, Spike responses to somatic current injection
757 just above the threshold current for the control and 2x[K^+]. The injected current and
758 membrane potential were specified for each trace. Arrowheads indicate thresholds. **G**,
759 dV/dt, and membrane potential relationship of the action potential in **F**. Arrowheads
760 indicate the threshold voltage. **H–K**, Threshold current (**H**), threshold voltage (**I**),
761 amplitude (**J**), and maximum dV/dt (**K**) of spikes. Resting membrane potential was –
762 63.8±0.7 mV (n = 17) and –67.1±0.7 mV (n = 18) ($p < 0.01$) for control and 2x[K^+],
763 respectively. **L, M**, Spontaneous activities recorded under a current clamp without (**L**)
764 and with (**M**) DTX (40 nM). Spontaneous spike bursts appeared in the control but not in

765 the 2x[K^+]-treated neurons (10 s). The numbers in parentheses indicate the number of
766 cells. * $p < 0.05$, ** $p < 0.01$ by Student's *t*-test.
767
768 **Figure 4 AIS shortening occurred via activation of glutamate receptors and Cav**
769 **channels**
770 **A**, Time course of the experiments. HCF slices were incubated with blockers of
771 glutamate receptors, Cav channels in a 2x[K^+] medium, or with an activator in a normal
772 (1x[K^+]) medium for 7–10DIV. **B**, Schematic drawing of Ca^{2+} sources in NM neurons.
773 **C**, AIS of NM neurons. **D–F**, Length of AIS. The numbers in parentheses indicate the
774 number of cells. The AIS lengths for 1x[K^+] (light gray) and 2x[K^+] (green) media are
775 from Fig. 1F (10DIV) and 2I, respectively. **G**, Effects of Cav channel blockers on
776 spontaneous spikes recorded under a cell-attached clamp in ACSF containing 10 mM
777 KCl. **H**, Spontaneous spikes are occluded by a cocktail of P/Q- and N-type Cav channel
778 blockers. ** $p < 0.01$ compared with 2x[K^+] (**D, F**) by Kruskal-Wallis test, control (**H**)
779 by one-way ANOVA and *post-hoc* test, or by Student's *t*-test (**E**).
780
781 **Figure 5 AIS shortening occurred via activation of MEK and CDK5 pathways**
782 **A**, Time course of the experiments. HCF slices were incubated with kinase inhibitors in
783 a 2x[K^+] medium or with activators in a normal (1x[K^+]) medium for 7–10DIV. **B**,
784 MEK signaling pathway. **C**, AIS of NM neurons. **D–F**, Length of AIS. Effects of kinase
785 inhibitors (**D**), concentration dependence of U0126 (**E**), and phosphatase inhibitors (**F**),
786 respectively in the 2x[K^+] medium. Control (2x[K^+], green) is from Fig. 2I. **G**,
787 Activators of PKA and PKC shortened AIS in the 1x[K^+] medium. Control (1x[K^+],
788 light gray) is from Fig. 1F. **H**, MEK or CDK5 inhibitors occluded AIS shortening by

forskolin (FSK) or PMA. AIS lengths for FSK and PMA alone (light gray) are from Fig. 5G. Numbers in parentheses indicate the number of cells. * $p < 0.05$, ** $p < 0.01$ compared with 2x[K^+] (**D–F**) by one-way ANOVA and *post-hoc* test, 1x[K^+] (**G**), FSK or PMA alone (**H**) by Kruskal-Wallis test.

Figure 6 AIS shortening occurred in a manner dependent on CDK5 activity

A, Time course of the experiments. Plasmids were introduced into NM neurons at E2, HCF slices were prepared at E11, and DOX was added to the culture medium at 6–10DIV. **B**, tdTomato (red) was expressed in NM neurons (ipsi) in slice culture stained with panNav antibody (white). Dotted line indicates the midline. **C–K**, AIS of NM neurons with (ipsi) or without (contra) overexpression of dnCDK5 in 2x[K^+] medium (**C**), and of CDK5 (**E**), p35 (**G**), p35(T138A) (**I**), or CDK5 and p35 (**K**) in normal (1x[K^+]) medium. Plasmids used are shown in each panel. Note the absence of Nav signals at AIS in CDK5 and p35 double-positive neurons (**K**, left). Intensity profiles of Nav signal are the average of 10 cells (**D, F, H, J**). **L, M**, Length of AIS in 2x[K^+] (**L**) and 1x[K^+] (**M**) media. Numbers in parentheses indicate the number of cells. **N**, Ratio of mRNA level of CDK5 and p35 between 2x[K^+] and 1x[K^+] media. Numbers in parentheses represent the number of experiments in (**N**). **O**, AIS length of NM neurons from LCF with (ipsi) or without (contra) overexpression of p35 in normal (1x[K^+]) medium. Plasmid in (**G**) was used. * $p < 0.05$, ** $p < 0.01$ compared with mock by Student's *t*-test (**L, N**) and one-way ANOVA and *post-hoc* test (**M**).

Figure 7 CDK5 mediated AIS shortening via reorganization of microtubules

812 **A**, Time course of the experiments. HCF slices were incubated with stabilizers of
813 microtubules (MT) or actin during treatment with 2x[K^+] medium, FSK or PMA, or
814 okadaic acid for 7–10DIV. **B**, Pharmacological manipulation of microtubule dynamics.
815 **C**, Effects of MT and actin filament stabilizers on AIS of NM neurons in 2x[K^+]
816 medium. **D, E**, MT stabilizers occluded AIS shortening by 2x[K^+] medium (**D,** left), by
817 FSK, PMA (**D,** right), or by okadaic acid (**E**). AIS lengths for 2x[K^+] (green), FSK or
818 PMA alone (light gray), and normal (1x[K^+]) medium (light gray) were from Fig. 2I,
819 5D, and 1F (10DIV), respectively. ** $p < 0.01$ compared with 2x[K^+] (**D,** left), 1x[K^+]
820 (**E**) by one-way ANOVA and *post-hoc* test, FSK or PMA alone (**D,** right) by Kruskal-
821 Wallis test. **F–I**, Taxol occluded AIS shortening by overexpression of p35 (**G**) or p35
822 together with CDK5 (**H**). Time course of experiments (**F**) and AIS length (**I**). p35 and
823 p35 together with CDK5 are from Fig. 6M. ** $p < 0.01$ by Student's *t*-test. Numbers in
824 parentheses indicate the number of cells.
825

Fig.1

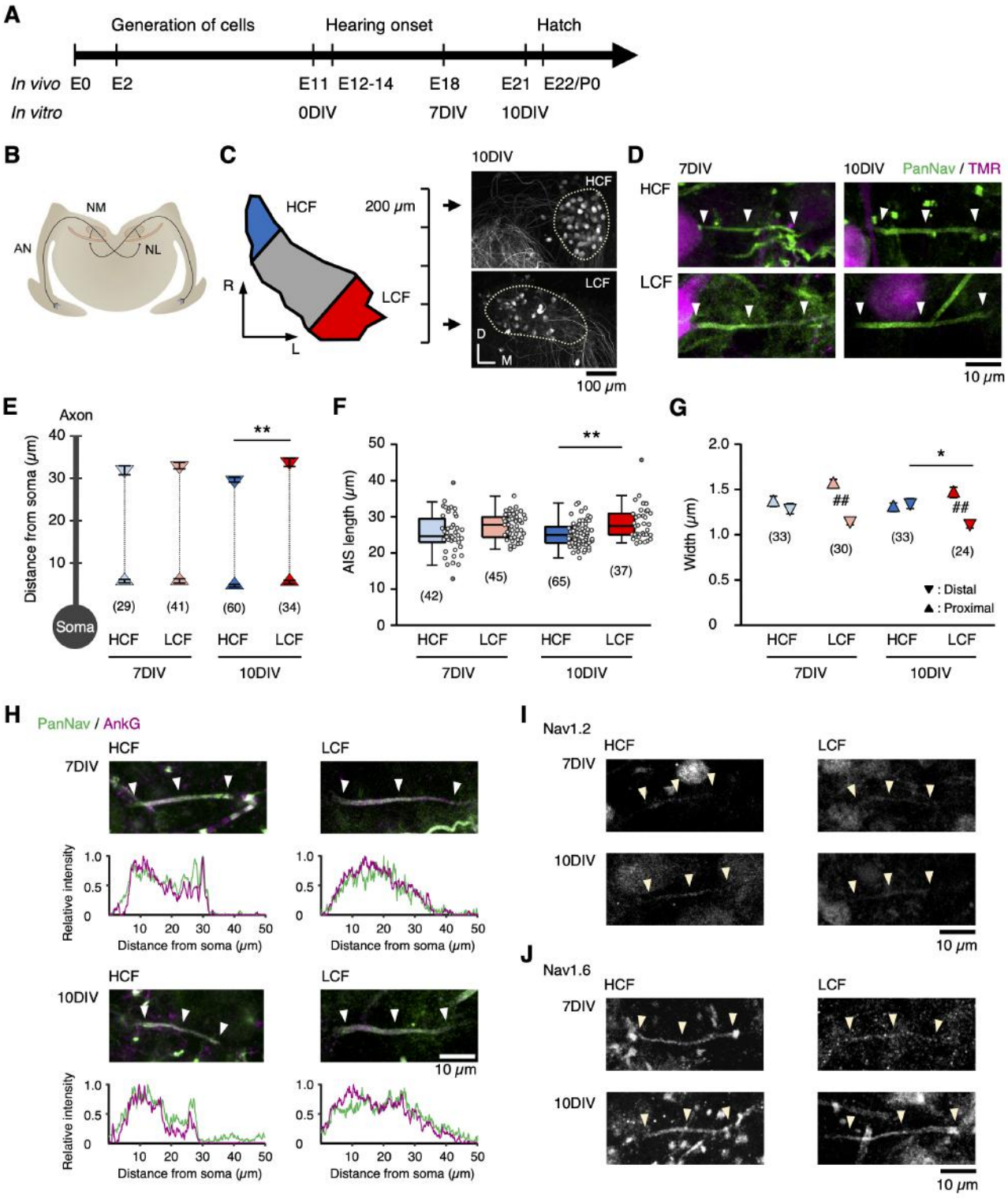
A
Generation of cells
Hearing onset
Hatch
In vivo E0 E2 E11 E12-14 E18 E21 E22/P0
In vitro 0DIV 7DIV 10DIV
B
NM
AN
NL
C
HCF
LCF
200 μm
R
L
10DIV
D
M
100 μm
D
7DIV
10DIV
PanNav / TMR
10 μm
E
Axon
Distance from soma (μm)
Soma
(29) (41) (60) (34)
HCF LCF HCF LCF
7DIV 10DIV
F
AIS length (μm)
(42) (45) (65) (37)
G
Width (μm)
(33) (30) (33) (24)
▼ : Distal
▲ : Proximal
H
PanNav / AnkG
Relative intensity
Distance from soma (μm)
I
Nav1.2
J
Nav1.6

Fig.2

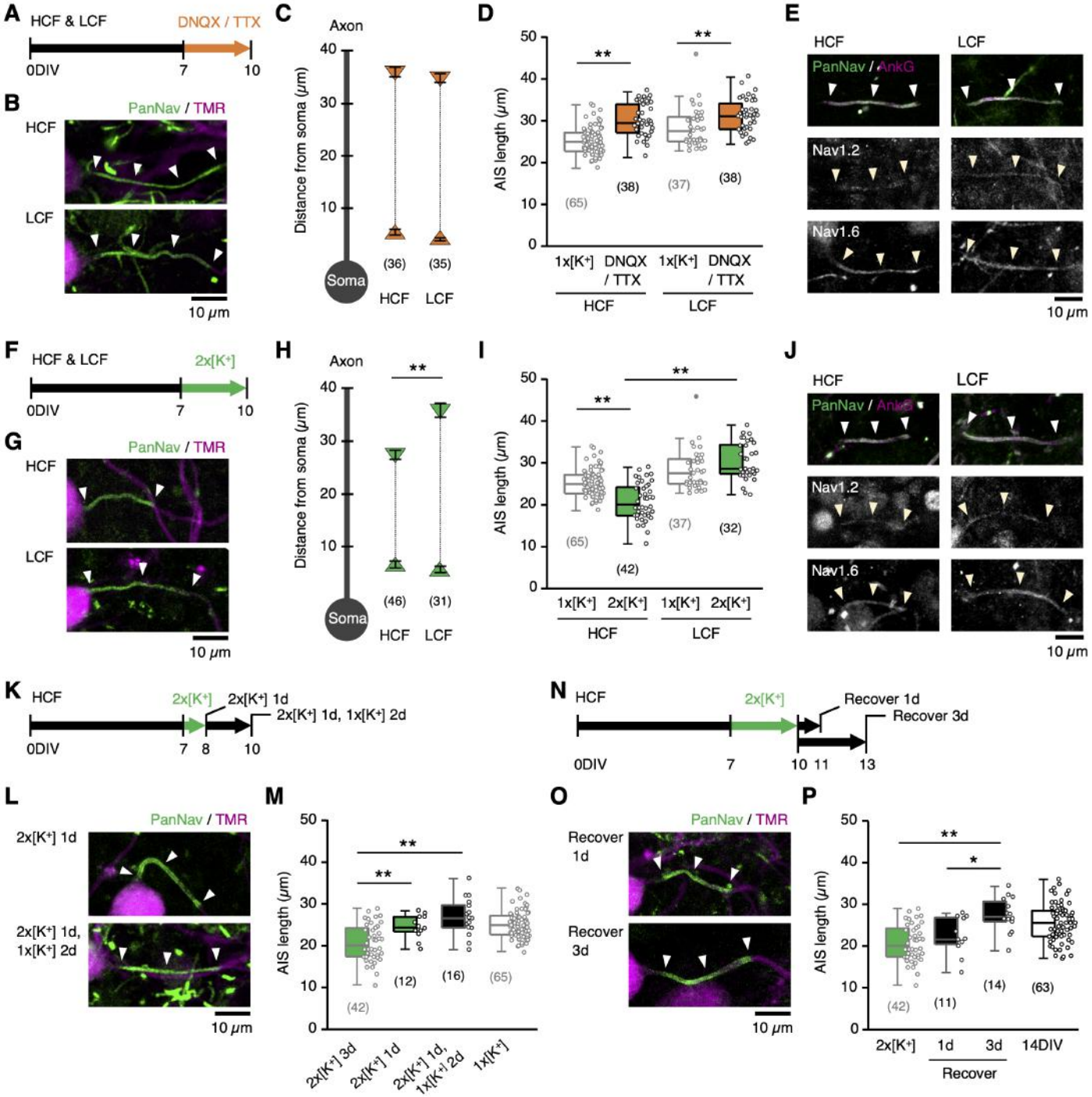
A
HCF & LCF
DNQX / TTX
0DIV
7
10
B
PanNav / TMR
HCF
LCF
10 μm
C
Axon
Distance from soma (μm)
Soma
(36)
(35)
HCF
LCF
D
AIS length (μm)
**
**
(65)
(38)
(37)
(38)
1x[K+]
DNQX / TTX
1x[K+]
DNQX / TTX
HCF
LCF
E
HCF
LCF
PanNav / AnkG
Nav1.2
Nav1.6
10 μm
F
HCF & LCF
2x[K+]
0DIV
7
10
G
PanNav / TMR
HCF
LCF
10 μm
H
Axon
**
Distance from soma (μm)
Soma
(46)
(31)
HCF
LCF
I
AIS length (μm)
**
**
(65)
(42)
(37)
(32)
1x[K+]
2x[K+]
1x[K+]
2x[K+]
HCF
LCF
J
HCF
LCF
PanNav / AnkG
Nav1.2
Nav1.6
10 μm
K
HCF
2x[K+]
2x[K+] 1d
2x[K+] 1d, 1x[K+] 2d
0DIV
7
8
10
N
HCF
2x[K+]
Recover 1d
Recover 3d
0DIV
7
10
11
13
L
PanNav / TMR
2x[K+] 1d
2x[K+] 1d, 1x[K+] 2d
10 μm
M
AIS length (μm)
**
**
(42)
(12)
(16)
(65)
2x[K+] 3d
2x[K+] 1d
2x[K+] 1d, 1x[K+] 2d
1x[K+]
O
PanNav / TMR
Recover 1d
Recover 3d
10 μm
P
AIS length (μm)
**
*
(42)
(11)
(14)
(63)
2x[K+]
1d
3d
14DIV
Recover

Fig.3

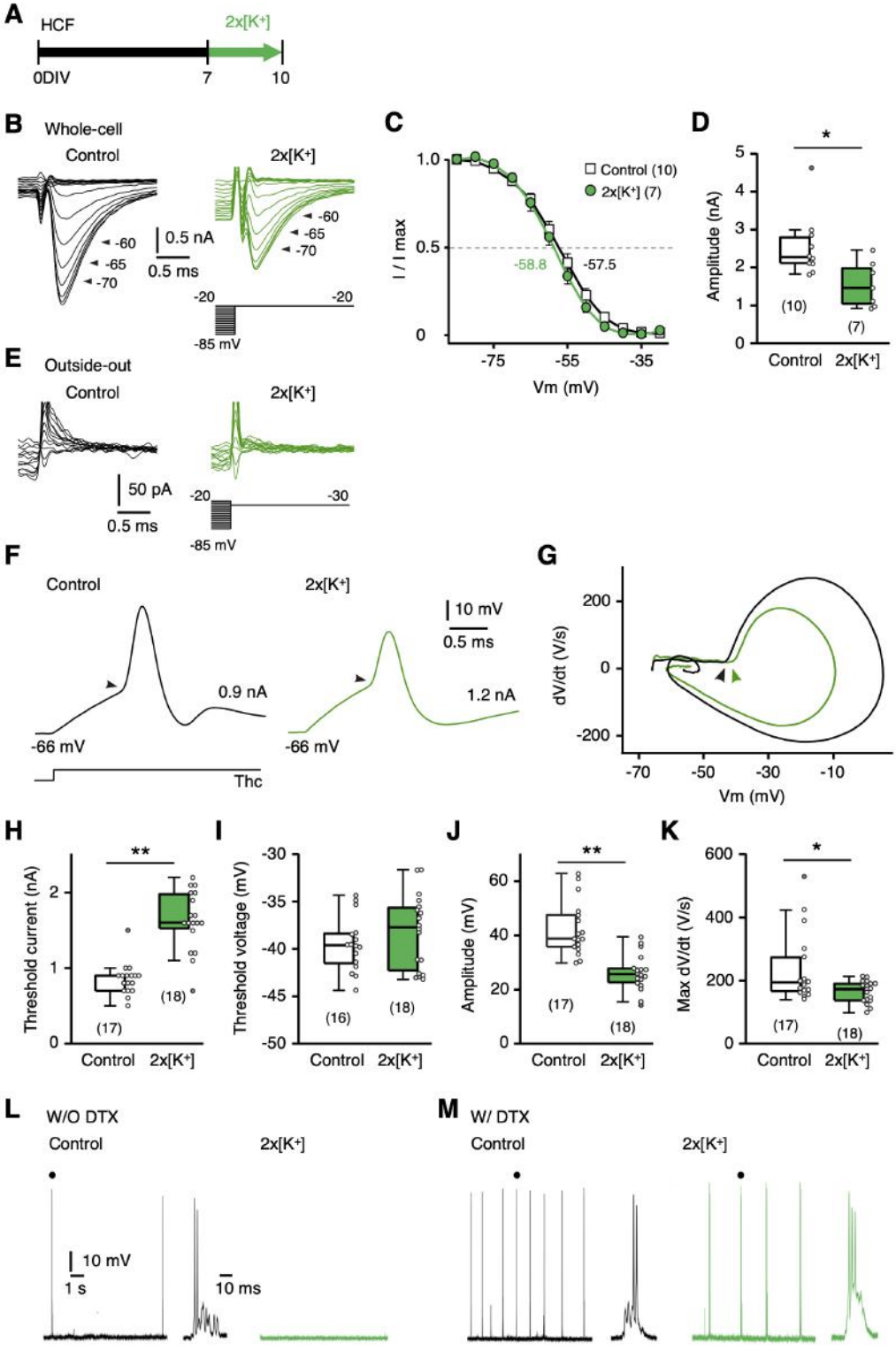
A
HCF
2x[K+]
0DIV
7
10
B
Whole-cell
Control
2x[K+]
-60
-65
-70
0.5 nA
0.5 ms
-20
-85 mV
C
Control (10)
2x[K+] (7)
I / I max
-58.8
-57.5
Vm (mV)
D
Amplitude (nA)
(10)
(7)
Control
2x[K+]
E
Outside-out
50 pA
0.5 ms
-30
F
10 mV
0.5 ms
0.9 nA
1.2 nA
-66 mV
Thc
G
dV/dt (V/s)
Vm (mV)
H
Threshold current (nA)
I
Threshold voltage (mV)
J
Amplitude (mV)
K
Max dV/dt (V/s)
L
W/O DTX
10 mV
1 s
10 ms
M
W/ DTX

Fig.4

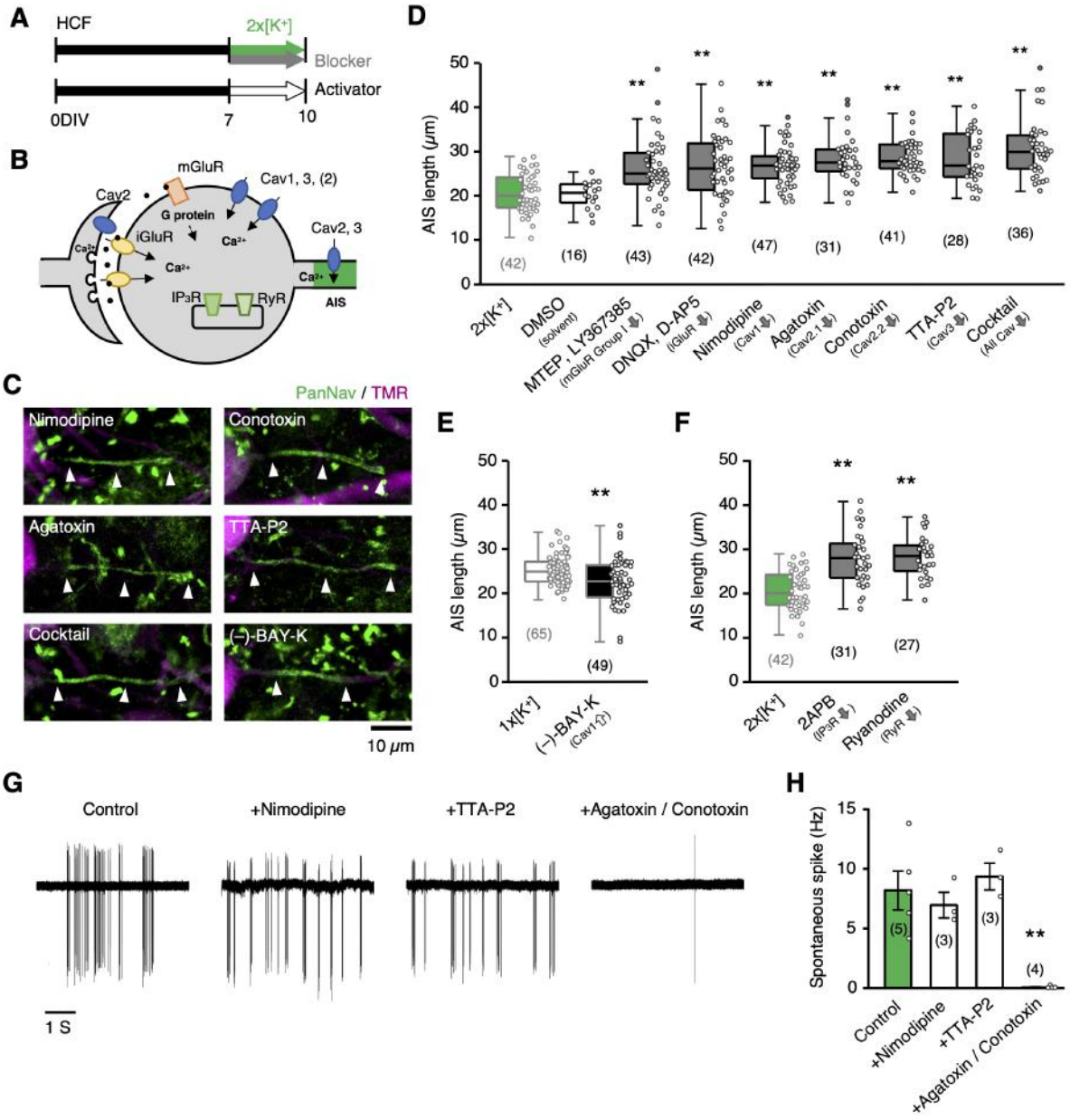
A
HCF
2x[K+]
Blocker
Activator
0DIV
7
10
B
mGluR
Cav1, 3, (2)
Cav2
G protein
iGluR
Ca2+
Cav2, 3
IP3R
RyR
AIS
C
PanNav / TMR
Nimodipine
Conotoxin
Agatoxin
TTA-P2
Cocktail
(−)-BAY-K
10 μm
D
AIS length (μm)
2x[K+]
DMSO (solvent)
MTEP, LY367385 (mGluR Group I)
DNQX, D-AP5 (iGluR)
Nimodipine (Cav1)
Agatoxin (Cav2.1)
Conotoxin (Cav2.2)
TTA-P2 (Cav3)
Cocktail (All Cav)
E
AIS length (μm)
1x[K+]
(−)-BAY-K (Cav1)
F
AIS length (μm)
2x[K+]
2APB (IP3R)
Ryanodine (RyR)
G
Control
+Nimodipine
+TTA-P2
+Agatoxin / Conotoxin
1 S
H
Spontaneous spike (Hz)
Control
+Nimodipine
+TTA-P2
+Agatoxin / Conotoxin

Fig.5

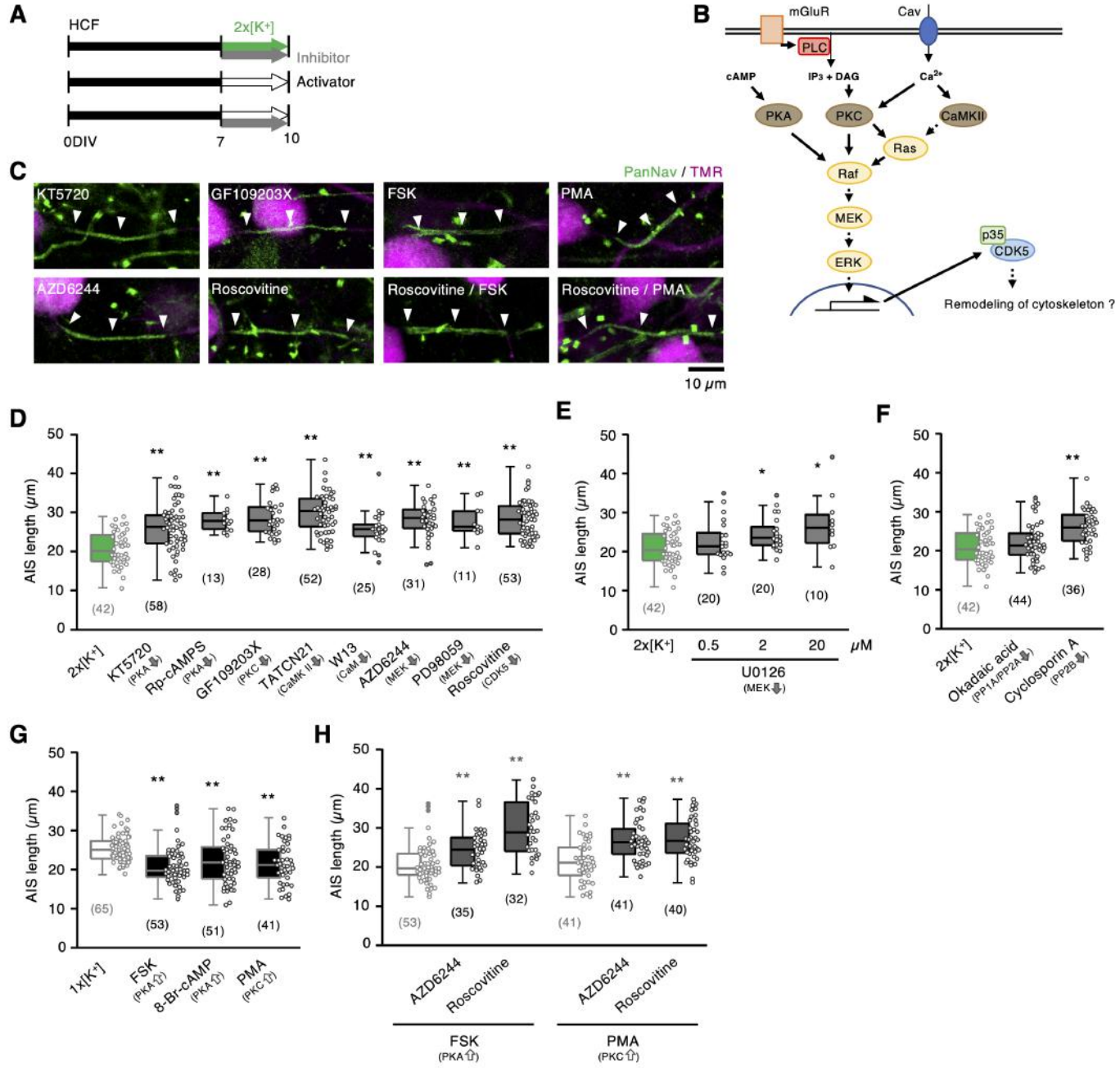
A
HCF
2x[K+]
Inhibitor
Activator
0DIV
7
10
B
mGluR
Cav
PLC
cAMP
IP3 + DAG
Ca2+
PKA
PKC
CaMKII
Ras
Raf
MEK
ERK
p35
CDK5
Remodeling of cytoskeleton ?
C
PanNav / TMR
KT5720
GF109203X
FSK
PMA
AZD6244
Roscovitine
Roscovitine / FSK
Roscovitine / PMA
10 μm
D
AIS length (μm)
2x[K+]
KT5720 (PKA)
Rp-cAMPS (PKA)
GF109203X (PKC)
TATCN21 (CaMK II)
W13 (CaM)
AZD6244 (MEK)
PD98059 (MEK)
Roscovitine (CDK5)
E
AIS length (μm)
2x[K+]
0.5
2
20
μM
U0126 (MEK)
F
AIS length (μm)
2x[K+]
Okadaic acid (PP1A/PP2A)
Cyclosporin A (PP2B)
G
AIS length (μm)
1x[K+]
FSK (PKA)
8-Br-cAMP (PKA)
PMA (PKC)
H
AIS length (μm)
AZD6244
Roscovitine
AZD6244
Roscovitine
FSK (PKA)
PMA (PKC)

Fig.6

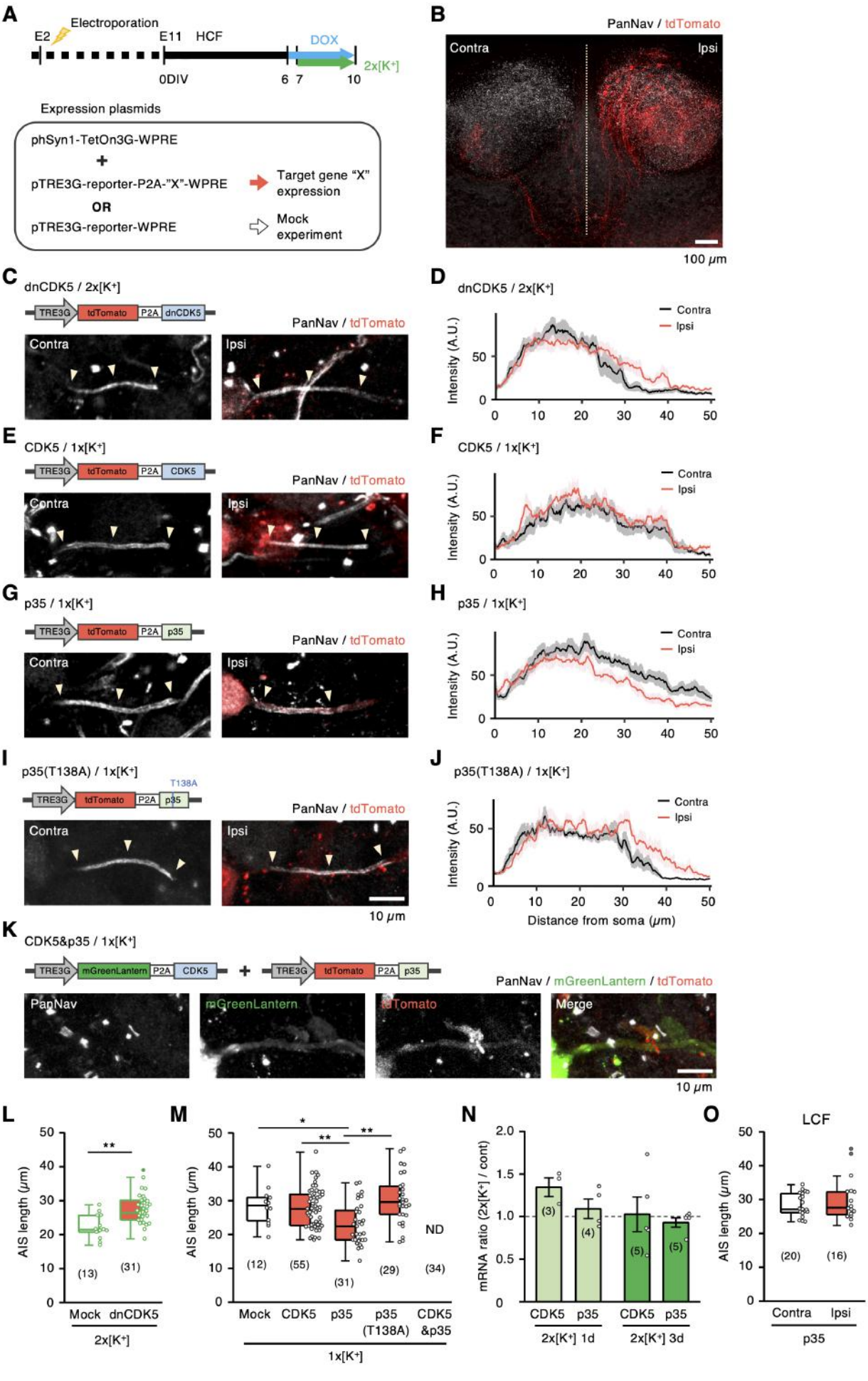
A
Electroporation
E2
E11
HCF
DOX
2x[K+]
0DIV
6 7
10
Expression plasmids
phSyn1-TetOn3G-WPRE
+
pTRE3G-reporter-P2A-"X"-WPRE
OR
pTRE3G-reporter-WPRE
Target gene "X" expression
Mock experiment
B
PanNav / tdTomato
Contra
Ipsi
100 μm
C
dnCDK5 / 2x[K+]
TRE3G
tdTomato
P2A
dnCDK5
PanNav / tdTomato
Contra
Ipsi
D
dnCDK5 / 2x[K+]
Contra
Ipsi
Intensity (A.U.)
E
CDK5 / 1x[K+]
CDK5
F
CDK5 / 1x[K+]
G
p35 / 1x[K+]
p35
H
p35 / 1x[K+]
I
p35(T138A) / 1x[K+]
T138A
J
p35(T138A) / 1x[K+]
Distance from soma (μm)
K
CDK5&p35 / 1x[K+]
mGreenLantern
PanNav / mGreenLantern / tdTomato
PanNav
mGreenLantern
tdTomato
Merge
10 μm
L
AIS length (μm)
Mock
dnCDK5
2x[K+]
M
Mock
CDK5
p35
p35 (T138A)
CDK5 &p35
ND
1x[K+]
N
mRNA ratio (2x[K+] / cont)
CDK5
p35
2x[K+] 1d
2x[K+] 3d
O
LCF
Contra
Ipsi
p35

Fig.7

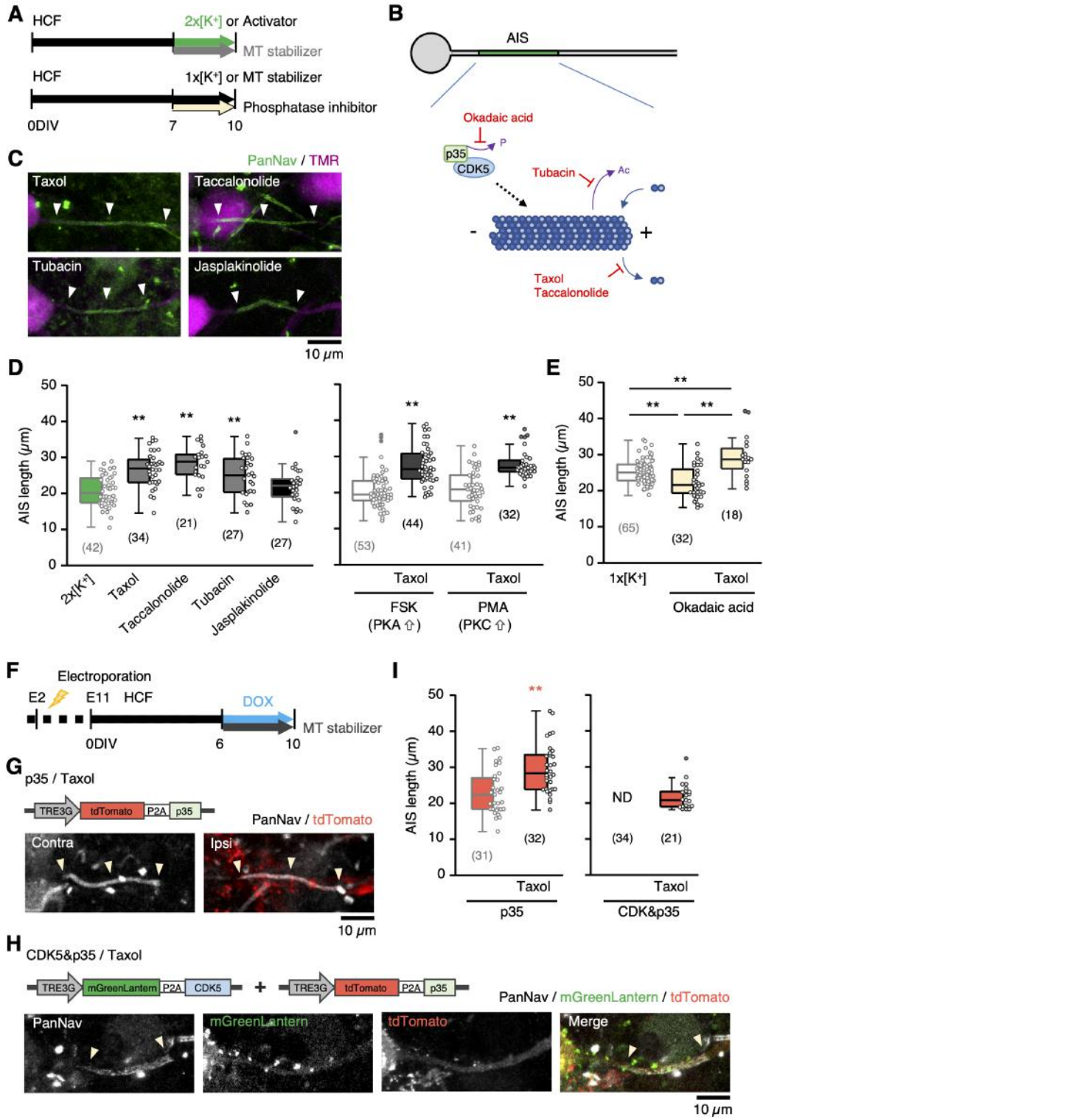
A
HCF
2x[K+] or Activator
MT stabilizer
HCF
1x[K+] or MT stabilizer
Phosphatase inhibitor
0DIV
7
10
B
AIS
Okadaic acid
P
p35
CDK5
Tubacin
Ac
-
+
Taxol
Taccalonolide
C
PanNav / TMR
Taxol
Taccalonolide
Tubacin
Jasplakinolide
10 μm
D
AIS length (μm)
2x[K+]
Taxol
Taccalonolide
Tubacin
Jasplakinolide
FSK (PKA ⇧)
PMA (PKC ⇧)
E
1x[K+]
Okadaic acid
F
Electroporation
E2
E11
HCF
DOX
MT stabilizer
0DIV
6
10
G
p35 / Taxol
TRE3G
tdTomato
P2A
p35
PanNav / tdTomato
Contra
Ipsi
10 μm
H
CDK5&p35 / Taxol
TRE3G
mGreenLantern
P2A
CDK5
TRE3G
tdTomato
P2A
p35
PanNav / mGreenLantern / tdTomato
PanNav
mGreenLantern
tdTomato
Merge
10 μm
I
AIS length (μm)
p35
CDK&p35
ND